AIAA Journal
Vol. 39, No. 1, January 2001

Flow Visualizations and Measurements of a Three-Dimensional Supersonic Separated Flow

Brad A. Boswell* and J. Craig Dutton†
University of Illinois at Urbana–Champaign, Urbana, Illinois 61801

The flow along the afterbody and in the base region of a circular cylinder with a length-to-radius ratio of 3.0 aligned at a 10-deg angle of attack to a nominal Mach 2.5 freestream has been investigated experimentally. The objective is to better understand the mechanisms that control base flow for supersonic bodies with a nonzero-angle-of-attack orientation. Laser Doppler velocimetry measurements were conducted in the incoming boundary layer to quantify the initial conditions at the onset of three-dimensional behavior. Schlieren and Mie scattering visualizations were obtained to discern governing flow features and to image the large-scale turbulent structures of this separated flow. Surface oil-streak visualizations were obtained to determine the three dimensionality of the afterbody surface flow and to deduce the base surface flowfield. Pressure-sensitive paint measurements were completed to determine the spatial evolution of surface pressure along the cylindrical body at angle of attack and to determine the change in base pressure caused by inclination of the body. Results provide evidence of expected mean-flow features, including base-corner expansions, separated shear layer development, recompression shocks, and a turbulent wake. No evidence of lee-side flow separation was detected along the afterbody. However, a strong secondary circumferential flow, which develops along the afterbody due to pressure gradients on its surface, results in the entrainment of fluid into the base region from the leeward portion of the flow. The average base pressure ratio measured for the angle of attack case is 48.4% lower than that measured for zero angle of attack, resulting in a significant increase in base drag for cylindrical objects inclined at angle of attack.

Nomenclature

A_n = fitting parameters
C_f = skin-friction coefficient
C_p = pressure coefficient
H = compressible shape factor, δ^*/θ
I = intensity of fluorescence
L = afterbody axial length
M = Mach number
p = static pressure
R = afterbody base radius
r = radial coordinate
r' = radial coordinate of approach flow
u_τ = friction velocity
V = mean velocity
x = axial coordinate
x' = axial coordinate of approach flow
z = spanwise coordinate
α = angle of attack
γ = ratio of specific heats
δ = boundary-layer thickness
δ^* = boundary-layer displacement thickness
θ = boundary-layer momentum thickness
ν_w = kinematic viscosity at the wall temperature
Π = boundary-layer wake strength parameter
ϕ = circumferential coordinate

Subscripts

b = base value
ref = reference value
x' = approach axial component
∞ = freestream value

Introduction

THE large contribution of base drag to the total drag about cylindrical bodies makes understanding of the fluid dynamic interactions that govern supersonic base flows critical to the improvement of aerodynamic vehicle performance. As a result, considerable effort has been expended not only to measure axisymmetric, supersonic base flows experimentally,[1–7] but also to model the flowfields numerically.[8–11] Although these previous studies provide detailed insight into the characteristics of a supersonic base flow at zero angle of attack, including boattail and base-bleed effects, this single test case does not account for all flight conditions experienced by supersonic vehicles. Rockets, missiles, and other aerodynamic vehicles spend a considerable portion of their flight paths oriented at nonzero angle of attack. In addition to the zero-angle-of-attack base flow features, three-dimensional effects are introduced during flight at angle of attack that significantly affect the flowfield behavior.

Figure 1 is a schematic of supersonic flow about a cylindrical sting with a sudden turn to a finite angle of attack α at some point along its length. Traditional supersonic base flow features during zero-angle-of-attack flight, such as expansion waves at the base-corner separation point, development of a compressible free shear layer, a base recirculation region, a series of recompression shocks, and a trailing wake also exist in this flow. In addition, for sufficiently large angle of attack and body length, counter-rotating symmetric vortex wakes will also develop on the lee side of the object.[12] For a given freestream Mach number, the strength of these lee-side vortices increases with body length-to-diameter ratio and angle of attack. Complete understanding of the fluid dynamic interactions between the three-dimensional afterbody flow and that in the base flow region is necessary to accurately predict flight performance.

Although detailed flow characteristics of the three-dimensional leeward vortices have been measured in previous studies,[12] interference from downstream model supports has resulted in limited accurate experimental pressure data in the base region for supersonic flight at angle of attack. In a review of supersonic base-pressure data at angle of attack, Lamb and Oberkampf[13] found only two experimental studies without interference effects. In the first study, completed by Pick,[14] the trajectories of cones launched into a hypersonic flow at varying angles of attack were recorded in a motion picture, which was then utilized to determine base pressure. The second study, completed by Moore et al.,[15] measured the base pressure

---

Received 10 December 1999; revision received 23 May 2000; accepted for publication 26 May 2000.

*Graduate Research Assistant, Department of Mechanical and Industrial Engineering, 1206 West Green Street. Student Member AIAA.

†W. Grafton and Lillian B. Wilkins Professor, Department of Mechanical and Industrial Engineering, 1206 West Green Street. Associate Fellow AIAA.

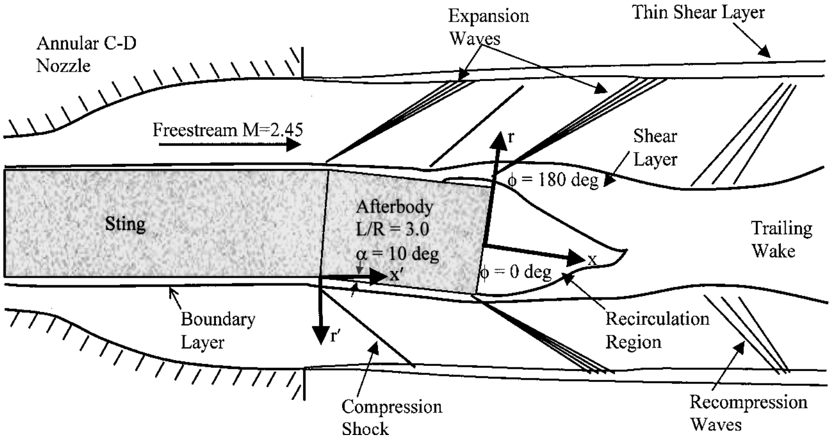

Fig. 1 Schematic of front sting-supported angle-of-attack afterbody and coordinate systems.

behind a cylindrical body with body length-to-radius ratio of 14.4 for varying angles of attack and freestream Mach numbers. Although these studies provide excellent pressure measurements at the base surface, that is essentially the limit of their contribution. To date, no detailed flowfield measurements have been completed to determine the fluid dynamic processes that control the behavior of a supersonic base flow at angle of attack.

This lack of detailed experimental flowfield data has hindered the efforts of numericists to validate computational models used in predicting base flow characteristics. In a recent review of numerical works, Sturek et al.[16] cited a number of computational studies that modeled the flowfield around cylindrical bodies at angle of attack. However, the results of these investigations were not extended to the base region due to a lack of experimental data for comparison. In addition, Sahu[17,18] has modeled base flow at angle of attack in the transonic flight regime and for various types of base cavities. These studies presented both velocity vector fields and Mach number contours in the base recirculation and wake regions of the flowfield. Clearly, detailed experimental data are needed to validate and improve computational models of this nature.

In the current investigation, experiments were conducted to visualize and measure the flowfield behind a cylindrical afterbody positioned at angle of attack in a supersonic flow. Two-component laser Doppler velocimeter (LDV) measurements of the incoming boundary layer are included to verify the interference-free nature of the approach flow and to provide initial conditions for computational modeling. Flowfield visualizations were obtained to provide a qualitative view of the general flow structure in the base region. In addition, surface-flow visualizations are included to depict the flow pattern along the afterbody and on the base itself. Finally, detailed pressure-sensitive paint measurements are presented along the afterbody and on the base surface, thus providing a means for comparison of base pressure to results measured at zero angle of attack.[3] These data will help to improve understanding of this complex, three-dimensional, compressible, separated flow and will aid in numerical modeling of supersonic base flows at angle of attack.

Experimental Facilities and Procedures

All experiments were conducted in the University of Illinois Gas Dynamics Laboratory in a blow-down-type supersonic wind tunnel designed specifically for axisymmetric base flows. In this facility, compressed air passes from a stagnation chamber, through a combination screen–honeycomb flow conditioning section, and into an annular converging–diverging (C–D) nozzle to reach supersonic conditions. The supersonic freestream flow then passes into the test section before finally exiting through a conical diffuser into a silencing duct. A hollow, annular sting, aligned on the tunnel centerline, is supported far upstream of the nozzle to prevent support interference effects in the supersonic region of the tunnel (see Fig. 1). The experimental afterbody is attached to the downstream end of the sting via internal threads and consists of a 63.5-mm-diam cylindrical base inclined to create a 10-deg-angle-of-attack afterbody with a length-to-radius ratio of 3.0. The afterbody is fabricated of brass (alloy 360) and is machined to a surface roughness of approximately 0.25 μm. During run-on conditions, it is estimated that the asymmetric pressure field creates at most a 35-μm deflection of the afterbody. Optical access to the afterbody and near-wake regions is available from three sides of the test section to allow for nonintrusive measurements and visualizations. A complete description of this facility is included in Ref. 19. The mass flow rate (approximately 7 kg/s) of this tunnel and stagnation pressure (approximately 565 kPa absolute) needed to maintain matched pressure conditions at the C–D nozzle exit prevents tunnel run times from exceeding 25 s.

A schematic of the experimental afterbody inside the axisymmetric nozzle is shown in Fig. 1. A cylindrical coordinate system is generally used in the presentation of the current results with the origin at the base center. Axial x displacement is measured along the normal to the base with positive values oriented in the downstream direction. Radial distance r is measured outward from the base center. Circumferential angle ϕ is measured from 0 deg on the windward to 180 deg on the leeward side of the afterbody in a clockwise (when looking downstream) direction. For incoming boundary-layer velocity profiles, a modified streamwise–transverse coordinate system (x'–r') is aligned with the incoming freestream, and its origin is placed at the angular discontinuity. Because the angular discontinuity position varies circumferentially (the afterbody is actually longer on the lee side than the windward side to create a smooth joint at the 10-deg discontinuity), the position where $x' = 0$ corresponds to the location where the angular discontinuity exists in the plane of interest for a particular measurement.

Conventional schlieren photography, using a 1.4-μs duration spark light source, was utilized to investigate the general features of the base-region flowfield and to ensure that no interference effects were present in the wind tunnel during operation. More detailed views of the near-wake flow structure were obtained using a Mie scattering technique similar to that utilized by Smith and Dutton.[20] In this visualization method, ethanol is injected far upstream of the C–D nozzle, where it vaporizes and mixes with the carrier air, and is then condensed into approximately 0.05-μm-diam droplets during acceleration to supersonic speeds in the annular C–D nozzle. These droplets are easily small enough to track the accelerations in this high-speed separated flow.[20] A Nd:Yag laser with beam-shaping optics is used to form a laser sheet that illuminates a thin plane (approximately 200 μm thickness) of the ethanol mist for 6–8 ns per laser pulse. This short illumination time effectively freezes the turbulent structures in space and allows for quasi-instantaneous images of the flowfield to be captured with a 14-bit, high-resolution, unintensified charge-coupled device (CCD) camera. Approximately 30 images were acquired at each spatial location to create ensemble-average images and to ensure that flow features in individual instantaneous images were representative of the general flow structure.

The two-component LDV system used in these experiments is almost identical to the system used in previous supersonic base flow studies conducted in the Gas Dynamics Laboratory.[3-6] The incoming flow was seeded by injection of silicone oil droplets upstream of the C–D nozzle to prevent interference effects from the injectors in the supersonic flow. This injection system has been shown to provide droplets with a nominal 0.8-μm diam, which is small enough for accurate fluid velocity measurements.[21] The four-beam crossing forms a probe volume 165 μm in diameter with green and blue beam fringe spacing of 14.5 and 13.6 μm, respectively. The beam pairs were rotated to ±45 deg from the freestream flow direction to prevent fringe blindness. In addition, Bragg cells provided a 40-MHz frequency shift to the downstream beam of each pair to allow a clear distinction between forward and reverse flow. Scattered light was collected with 20-deg off-axis forward-scatter receiving optics, resulting in an effective probe volume length of 700 μm. Photomultiplier tubes convert the scattered light intensity into an analog voltage, from which the Doppler frequencies and velocities are obtained through the use of an IFA-750 autocorrelation processor. Velocity was measured at approximately 35 wall-normal positions in each boundary-layer profile, with 4000 instantaneous velocity measurements made at each spatial location to compute turbulent velocity statistics. The probe volume was physically positioned with a computer-controlled, three-axis traverse table capable of 0.75-μm spatial resolution in each direction. For the incoming freestream velocity of $V_\infty = 573$ m/s, previous uncertainty analysis of these two-component LDV measurements[19] has estimated worst-case uncertainties of 1.2% of V_∞ in the mean velocity measurements and 2.3% of V_∞ in the rms velocity fluctuation measurements.

Oil-streak visualizations were used to determine the surface streakline pattern both along the afterbody and on the base itself. In this experimental technique, a carrier fluid is mixed with lampblack and is applied to the surface of interest. During experimental operation, the carrier fluid flows under the action of the surface shear stress distribution and eventually evaporates, leaving the lampblack on the surface as an indication of surface flow direction. For the current experiments, the liquid used for the afterbody visualizations was a combination of 50% Three-in-One oil and lampblack. For base-surface visualizations, a combination of 50% diesel fuel and lampblack was used because the lower pressure in this region required a more volatile carrier fluid for complete evaporation during the wind tunnel's maximum allowable run time. The surface-flow visualizations were photographed using standard, 100-speed, 35-mm film.

A series of 1.59-mm-diam pressure taps was placed on the afterbody model to obtain static pressure measurements along both the afterbody and base surfaces. On the base, 17 pressure taps were located, with half of the taps located on the diameter between $\phi = 0$ and 180 deg, and with the other half located on the diameter between $\phi = -90$ and 90 deg. The spacing between each base tap is 6.35 mm. On the afterbody surface, 20 taps are located, with 5 taps each located along the $\phi = 0$, 90, -90, and 180 deg longitudinal axes. Eight circumferentially equally spaced taps were positioned upstream of the angle-of-attack joint (Fig. 1) to verify that a uniform pressure field exists prior to the 10-deg afterbody turn. Mean static pressures were measured using a Pressure Systems, Inc., digital pressure transmitter (DPT 6400-T). Although the pressure taps provide some surface pressure data, pressure-sensitive paint (PSP) measurements were also completed to increase the spatial resolution of surface pressure data and to allow for measurements of surface pressure closer to the afterbody edges than possible with static taps.

PSP techniques have been used by a number of researchers[22-24] to measure surface pressure variations with much greater spatial resolution than possible with static taps. In this experiment, the pressure tap data provided a calibration for in situ surface-pressure measurements using a PSP technique similar to that of Woodmansee and Dutton.[24] This method uses the following relationship between surface pressure and the intensity of fluorescence for a luminescent coating on the surface, where A_1, A_2, and A_3 are fitting parameters:

$$p/p_{\text{ref}} = A_1 + A_2(I_{\text{ref}}/I) + A_3(I_{\text{ref}}/I)^2 \qquad (1)$$

By the use of the data collected at each pressure tap as a reference value, the least-squares fitting parameters can be calculated and then applied to the luminescent intensity field of the PSP to determine the pressure at any point.

The PSP compound used in this study was developed at Old Dominion University and is made up of 85% 1,1,1-trichloroethane, 15% GE RTV 118, and 300 ppm ruthenium bathophenanthroline chloride probe molecules.[24] The PSP-coated afterbody and base surfaces were excited using 450-nm filtered light from two tungsten-halogen light sources. The tunnel-off (reference) and tunnel-on fluorescence intensities were recorded using a 14-bit, high-resolution, unintensified CCD camera fitted with a 600-nm bandpass filter. Although the response time of the paint is too long compared to the turbulent timescales of this flow to allow for measurement of pressure fluctuations, ensembles of 20 images were averaged to ensure that the mean pressure field is represented correctly in the results. The uncertainty of the PSP measurements is estimated as less than 3% of the pressure ratio p/p_∞ at the location of the measurement. This estimate is based on a previous study using the same PSP formulation.[25]

Results and Discussion

Approach Boundary-Layer Velocity Measurements

Nine separate boundary-layer velocity profiles were measured prior to the angular discontinuity, with three profiles each measured in the $\phi = 0$, 90, and 180 deg circumferential planes. All of these velocity profiles show a fully developed compressible turbulent boundary layer with no apparent interference waves. These experimental data were curve fit using the method of Sun and Childs[26] for turbulent, compressible boundary layers. The resulting curve fit for the boundary layer measured at $\phi = 90$ deg and $x'/R = -0.031$ is shown in Fig. 2 in wall coordinates and is representative of all of the other boundary-layer profiles measured about the afterbody. Using the curve-fit results, boundary-layer parameters and integral thicknesses were determined. The average of these nondimensional values for the three axial stations measured at $x'/R = -0.031$ is included in Fig. 2. These nondimensional values are consistent with those previously measured in fully developed, turbulent, compressible boundary layers.[3-6,27] For example, the measured boundary-layer thickness $\delta/R = 0.103$ compares favorably with the $\delta/R = 0.10$ value measured by LDV for the zero-angle-of-attack case.[3] The freestream Mach number was found to be 2.45 ± 1%, and the resulting unit Reynolds number was calculated as 56×10^6 m^{-1}. Streamwise turbulence intensities in the freestream were consistently less than 2%.

Schlieren and Mie Scattering Flow Visualizations

Figure 3 shows a composite schlieren photograph of the flow along the afterbody, in the base recirculation region, and in the

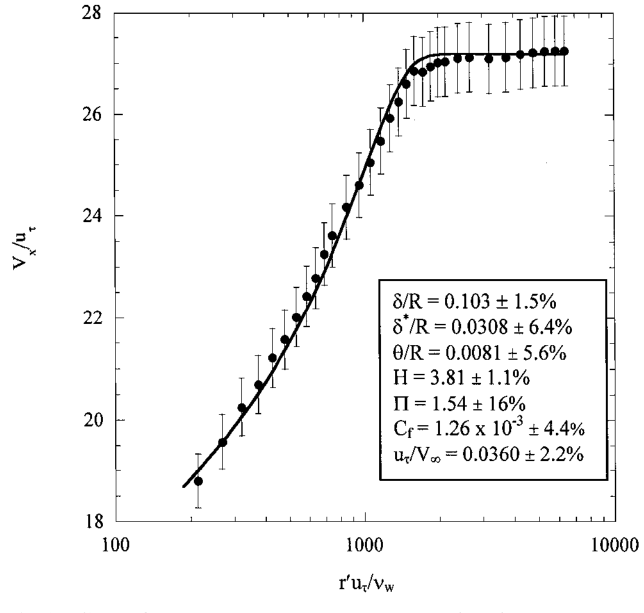

Fig. 2 Curve-fit and boundary-layer parameters for afterbody boundary layer upstream of angular discontinuity.

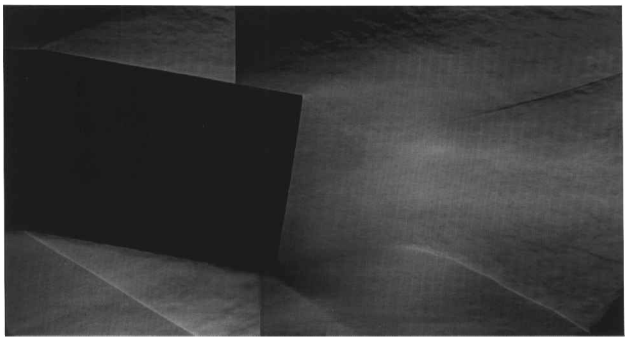

Fig. 3 Composite schlieren side-view photograph of flowfield.

near-wake region. Although some detail is lost in the photograph due to the three-dimensional nature of the flow, this image verifies the existence of many expected gasdynamic features. At the afterbody angular discontinuity, an oblique shock forms along the windward portion of the turn, while a Prandtl–Meyer expansion fan can be seen centered at the turn on the leeward edge. No lee-side boundary-layer separation is detected in the schlieren photograph. The fully attached boundary layer on the lee side results from the low length-to-radius ratio of the inclined afterbody for the given freestream Mach number and angle of attack. At the trailing edge of the afterbody, another Prandlt–Meyer expansion fan is found centered on both the windward and leeward base edges, similar to that in the zero-angle-of-attack case. The existence of expansion waves centered at the lee-side base corner provides additional evidence concerning the absence of boundary layer separation along the lee side of the afterbody. Farther downstream, the separated free shear layer can be visualized (seen only faintly due to three-dimensional effects), as can a recompression shock system and the trailing wake. Downstream of the base corner, the observed base flowfield structures are qualitatively similar to those found in zero-angle-of-attack flow but are rotated to an angle roughly corresponding to the afterbody angle of attack. From the location of the recompression shock system, it can be deduced that the length of the recirculation region enclosed by the free shear layer is quite short, which should correspond to a low base pressure and high base drag (discussed subsequently).

Although difficult to clearly discern in the schlieren images, the boundary-layer thickness may also be estimated along the afterbody. A thin boundary layer is seen on the windward surface due to compression by the oblique shock, with a visual thickness of approximately $\delta/R = 0.07$ at the base corner ($x/R = 0$). The boundary layer on the leeward side is difficult to discern, but appears to be much thicker, due to the expansion at the afterbody turn, with a visual thickness of approximately $\delta/R = 0.20$ at $x/R = 0$.

A composite Mie scattering side-view image of the free shear layer, recirculation region, and wake along the $\phi = 0$–180 deg plane is included in Fig. 4. This instantaneous side-view image shows all mean-flow structures observed in the average image and also provides a view of the turbulence structures representative of those seen throughout the ensemble. Similar to the conclusion from the schlieren images, the recirculation region appears much shorter than in the zero-angle-of-attack case, for which Herrin and Dutton[3] reported a rear stagnation point at $x/R = 2.65$, as determined by LDV measurements. Based on the apparent merger of supersonic flow from the leeward and windward sides of the afterbody, the stagnation point for this flow appears to occur at roughly $x/R \approx 1.7$. The instantaneous image also reveals the existence of large-scale turbulent structures along the shear layer and in the trailing wake. The turbulent structures in the shear layer are seen as filament-type structures extending into the darker recirculation region. The structures are much clearer in the trailing wake region, where individual structures appear as filaments elongated in the vertical direction. These structures appear to be qualitatively similar to those observed by Bourdon and Dutton[28] for supersonic axisymmetric base flow at zero angle of attack.

Additional large-scale structures of this type can be observed by rotating the laser sheet to expose the $\phi = 90/-90$ deg plane,

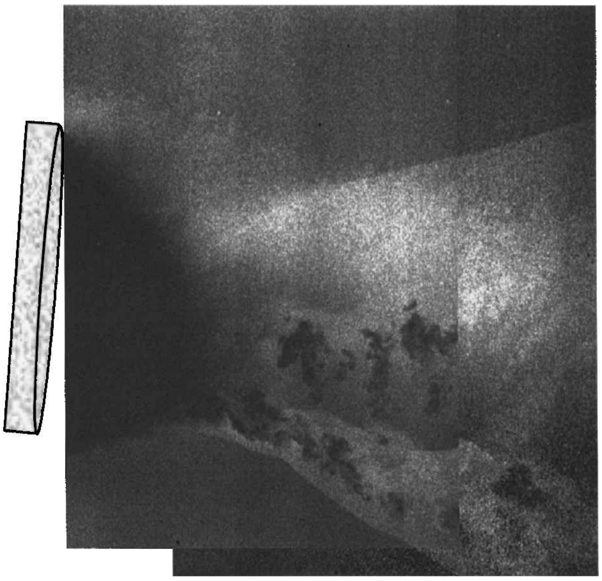

Fig. 4 Composite instantaneous Mie scattering side-view image of recirculation region and wake in the ϕ = 0/180 deg plane.

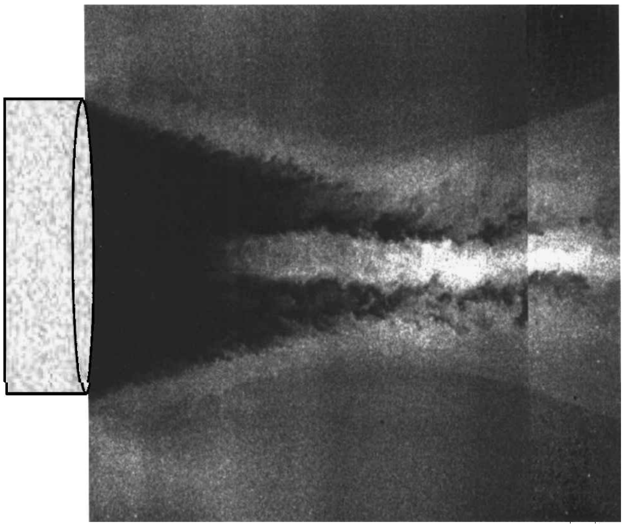

Fig. 5 Composite instantaneous Mie scattering side-view image of recirculation region and wake in the $\phi = -90/+90$ deg plane.

as seen in Fig. 5. The turbulent structures resemble those found in the $\phi = 0$–180 deg plane but appear to grow in size as the flow develops axially. In addition to the turbulent structure seen along the shear layer/recirculation region boundary and in the wake displayed in this view, Fig. 5 also shows the presence of entrained lee-side freestream fluid along the flow centerline (bright seeded region), with warmer recirculation fluid extending much farther downstream than suggested in the $\phi = 0$–180 deg side view (Fig. 4). The origin of the seeded fluid along the centerline in Fig. 5 will become clearer in the Mie scattering end views, which are discussed next.

Mie scattering end views at four streamwise locations downstream of separation are presented in Fig. 6, with the top of each image corresponding to the $\phi = 180$ deg (leeward) direction and with flow occurring out of the page. Although these images were obtained obliquely through the test section side windows, they have been rotated with image-processing software such that the mean-flow direction is normal to the page. These images suggest that the near-wake flow is highly three dimensional in nature, with two large recirculation lobes that divide the flow along the $\phi = 0$–180 deg axis and which decrease in size and become more elliptical as the flow moves downstream. These lobes develop because the flow along the afterbody is driven from the high-pressure windward side to the low-pressure leeward side as it moves downstream (see surface-flow

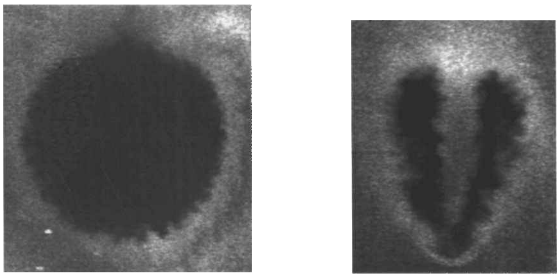

a) Instantaneous, $x/R = 0.75$ e) Instantaneous, $x/R = 1.5$

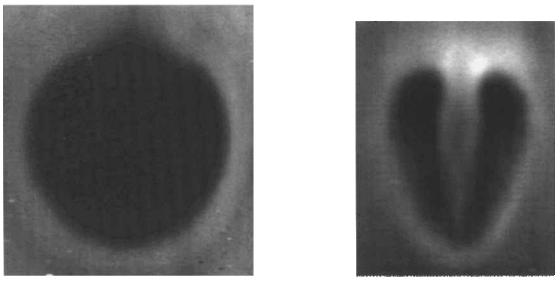

b) Average, $x/R = 0.75$ f) Average, $x/R = 1.5$

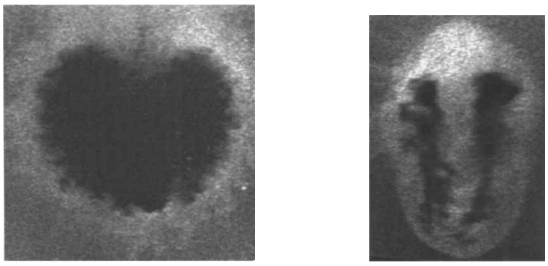

c) Instantaneous, $x/R = 1.0$ g) Instantaneous, $x/R = 2.0$

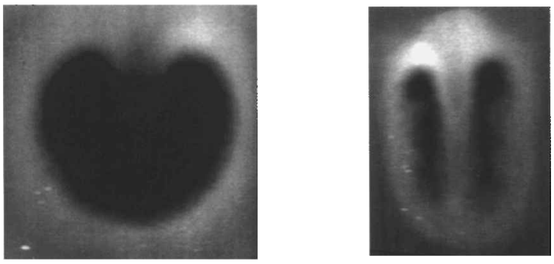

d) Average, $x/R = 1.0$ h) Average, $x/R = 2.0$

Fig. 6 Mie scattering instantaneous and average end-view images with approximate size of image a 50 × 45 mm and all other image sizes scaled to Fig. 6a.

visualizations to be presented). After separation of the boundary layer at the base corner, this rotation of fluid from windward to leeward continues with the fluid meeting at the $\phi = 180$ deg lee-side plane, where it is then driven down into the recirculation region. The separation between the lobes can be seen as the bright wedge of fluid moving downward into the dark recirculation region, until the lobes are completely closed off at a downstream distance of approximately $x/R = 1.7$. This lee-side fluid entrainment is the same phenomenon that was noted as a bright region along the centerline in the side view along the $\phi = 90/-90$ deg plane in Fig. 5. These persistent lobes seen in the end views suggest that the short wake recirculation region length compared to the zero-angle-of-attack case observed in the side-view schlieren (Fig. 3) and Mie scattering (Fig. 4) images is a phenomenon applicable primarily to the $\phi = 0/180$ deg plane.

In addition to these mean-flow features, the large-scale turbulent structures seen in these end views along the shear layer/recirculation region boundary appear qualitatively similar to those present in the zero-angle-of-attack case.[28] In particular, at $x/R = 1.5$ and 2.0, in the region where the rear stagnation point is suspected to occur, the number of structures observed around the shear layer periphery in the images varies from 10 to 16, corresponding to the 10 to 14 structures observed by Bourdon and Dutton[28] in the reattachment region of zero-angle-of-attack base flow. In both cases, the structures appear evenly spaced circumferentially about the shear layer. The slight increase in the number of structures for the current case is caused by the entrainment of lee-side fluid into the recirculation region, creating additional interface length on which more structures may form. Throughout the axial development of the flow, the number of these end-view structures decreases and their size increases as the flow moves downstream, indicating some kind of streamwise and/or helical structure amalgamation process.

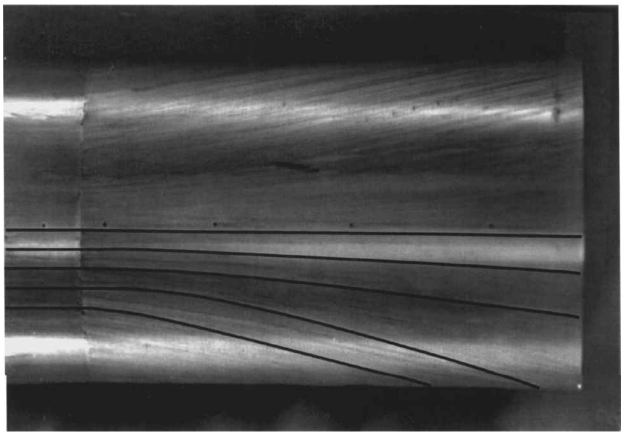

Fig. 7 Oil-streak visualization of $\phi = 0$ deg windward surface.

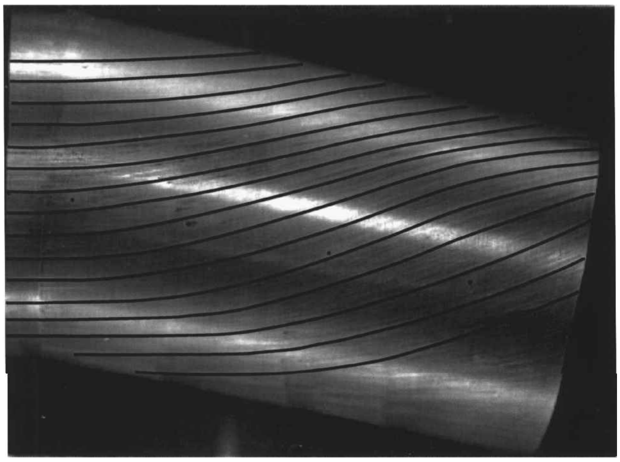

Fig. 8 Oil-streak visualization of $\phi = -90$ deg side surface.

Surface-Flow Visualizations

An oil-streak visualization of the $\phi = 0$ deg windward surface is included in Fig. 7. Lines have been drawn onto this and succeeding surface-flow photographs to help emphasize the streakline directions, which are sometimes rather faint. This oil-streak pattern shows the general structure of the surface flow, as fluid flows around the cylindrical body from the high-pressure windward portion of the afterbody toward the lower pressure leeward surface. This windward-to-leeward surface flow is most clearly seen in Fig. 8, which shows the oil-streak pattern for the $\phi = -90$ deg surface. This image clearly shows the highly three-dimensional aspects of the surface flow. Fluid originating near the windward surface at the upstream oblique shock is driven far into the leeward region by the end of the afterbody, a change in ϕ of nearly 90 deg along the afterbody length of $L/R = 3$. Figure 9 shows the surface flow on the $\phi = 180$ deg leeward surface, where the surface streaklines appear almost to converge near the base corner. The near convergence of surface streaklines results from the circumferential mass flow about the body from windward to leeward. For a long enough afterbody, this mass influx into the leeward region would result in flow separation from the afterbody. However, lee-side separation was not detected in the schlieren or Mie scattering images for the current afterbody length.

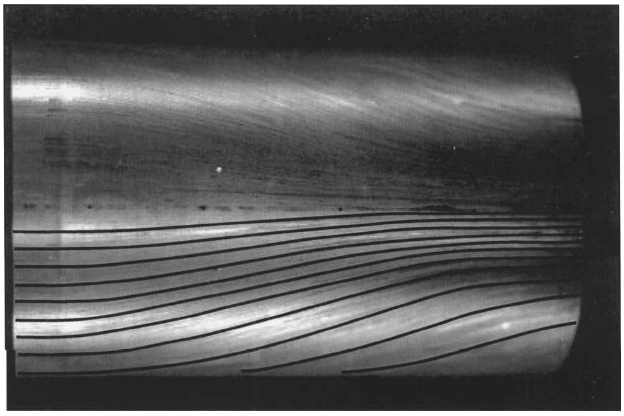

Fig. 9 Oil-streak visualization of $\phi = 180$ deg leeward surface.

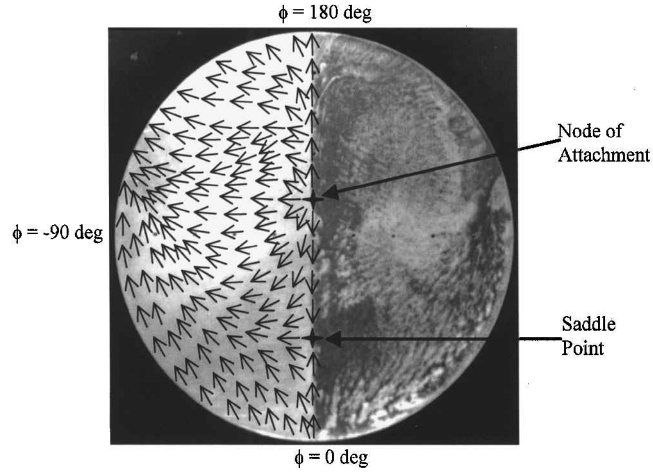

Fig. 10 Oil-streak visualization of base surface.

Figure 10 shows the surface flow on the base, with an oil-streak visualization included on the right side of the image, and the corresponding flow directions mapped on the left side of the image. The arrows drawn on the plot do not scale to velocity magnitudes for the base flow, but rather simply indicate the flow directions. The arrow directions were determined from many individual experiments in which discrete dots of the tracer were placed on the base and their temporal evolution was observed visually with the tunnel running. Two mathematical singularities were noted in this surface-flow pattern, a node of attachment along the $\phi = 0$–180 deg centerline just to the leeward side of the $\phi = +90/-90$ deg line, and a saddle point on the $\phi = 0$–180 deg symmetry line about halfway between the base center and the windward edge. The general structure of the base-surface flowfield consists of flow away from the symmetry line and surface flow from the windward-to-leeward edges. However, the node of attachment creates a region near the center of the afterbody where flow occurs from the leeward-to-windward regions. The surface flow appears to move radially outward along the base, across the afterbody edge, and then into the free shear layer in the circumferential region from $\phi = \pm 100$ to 180 deg, where the lowest surface pressures would be expected. Past research suggests that the number of nodes of separation and/or attachment must be at least two greater than the number of saddle points.[29] On this angle-of-attack base, the convergence of surface oil streaklines around the $\phi = \pm 120$ deg points near the base edge suggests that nodes or lines of separation would occur at both of these locations if the base radius was slightly larger. In fact, the regions of radially outward surface flow along the leeward surface edge of the base from $\phi = \pm 100$ to 180 deg effectively act as two nodes of separation on the base surface, thereby giving three attachment/separation nodes and one saddle point for the current base-surface flow. However, the presence of the base edge on this surface creates a discontinuity in the surface normal derivative that complicates the analysis of Tobak and Peake.[29]

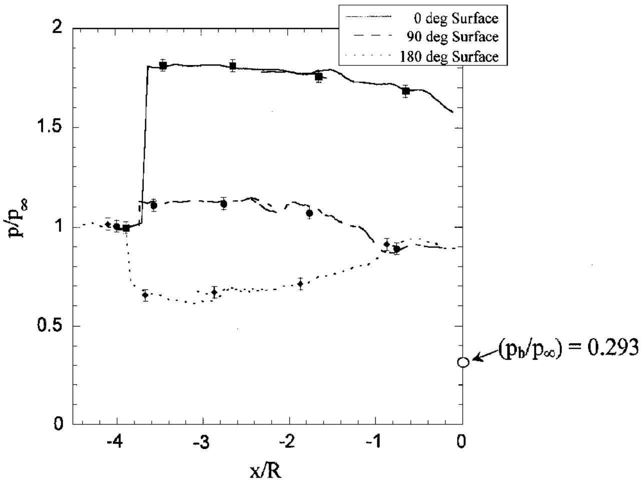

Fig. 11 Afterbody-surface streamwise pressure profiles.

Pressure Measurements

Surface-pressure-tap and PSP measurements were made upstream of the angular discontinuity to verify flow uniformity in this axisymmetric region. In addition, the surface-pressure measurements were continued along the afterbody itself to determine the pressure profiles along the $\phi = 0$, 90, and 180 deg surfaces. These results are presented in Fig. 11. To develop these profiles, 20-image ensembles were averaged, and the profile data were computed by averaging across five pixels (corresponding to the tap diameter in the images) in the circumferential direction. A Savitzky–Golay smoothing filter was utilized to remove high-frequency noise from the profiles, for which the minimum signal-to-noise ratio for any of the profiles was 44.6 on the $\phi = 180$ deg surface. As a result of this smoothing and the averaging of all available pressure tap data in computing the least-squares fitting parameters for Eq. (1), the PSP results do not pass directly through each pressure-tap data point. Because the afterbody PSP profiles were obtained in two images displaced axially from each other, a small region of overlap occurs in all three data sets. The regions of overlap have been included on all three distributions to demonstrate the repeatability of the data from the two views.

The surface pressures at the various circumferential positions upstream of the angular discontinuity are indeed relatively constant at the freestream value p_∞, providing a static-to-stagnation pressure ratio of 0.0621, corresponding to a freestream Mach number of 2.46. The $\phi = 0$ deg windward-side surface pressure increases substantially at the angular discontinuity due to the oblique compression shock and then decreases modestly along the afterbody length before reaching the trailing edge. The static pressure along this $\phi = 0$ deg surface significantly exceeds that of either the $\phi = 90$ or 180 deg surfaces everywhere along the afterbody length. On the $\phi = 180$ deg leeward surface, the surface static pressure drops across the expansion waves at the angular discontinuity, then increases along the afterbody surface up to the base corner. This increasing pressure along the leeward surface is the type of adverse pressure gradient that would lead to the eventual boundary-layer separation that is expected along this surface. In fact, the slight decrease in pressure at the very end of the $\phi = 180$ deg profile may suggest incipient separation just before the base corner. However, this decrease is within the experimental uncertainty of the PSP data ($U_{p/p_\infty} = \pm 0.04$) and is more likely explained by the pressure matching that occurs with the $\phi = 90$ deg plane (see Fig. 11). Along this $\phi = 90$ deg side plane, there is a slight increase in pressure at the angular discontinuity, suggesting a weak compression shock there. The static pressure then decreases modestly along the afterbody length on this surface, to match closely the lee-side pressure distribution just prior to the base corner. However, the average base pressure ratio, $(p_b/p_\infty) = 0.293$, is significantly less than the pressure immediately preceding separation of any of the measured afterbody pressure profiles.

The strong circumferential pressure gradient just downstream of the angular discontinuity indicated in Fig. 11 is clearly a major factor in the development of the three-dimensional structure of this separated flow. Along the afterbody surface, this pressure gradient drives a secondary flow from the high-pressure windward region toward the low-pressure leeward portion of the afterbody. This flow pattern is clearly seen in the earlier discussed surface-flow visualizations (Figs. 7–9). The presence of this windward-to-leeward secondary flow along the afterbody assists in the formation of the lee-side base vortices after separation, where the flow reaching the leeward side from both the positive and negative ϕ directions is then deflected into the base recirculation region, as suggested in the Mie scattering end views (Fig. 6).

Radial base pressure profiles along the $\phi = 0$, 90, and 180 deg radii are included in Fig. 12. Data reduction was completed in a manner identical to that used for the afterbody axial profiles, with only one modification. Profile data were computed by averaging eight pixels normal to the traverse direction because the image was zoomed in to a higher spatial resolution in the base image compared to the afterbody data. A base-surface pressure contour map is included in Fig. 13. The entire contour map was averaged across the $\phi = 0$–180 deg symmetry line, with the average pressure difference between symmetric pixels being $\Delta p / p_\infty = 0.0005$. Note that the ordinate scales p / p_∞ on these base pressure plots are highly expanded, so that the trends in the data only constitute small static pressure variations, well within the uncertainty of the PSP measurements. The circles seen along the $\phi = -90$–90 deg and 0–180 deg lines are due to imperfect masking of the pressure tap holes in the PSP data reduction process.

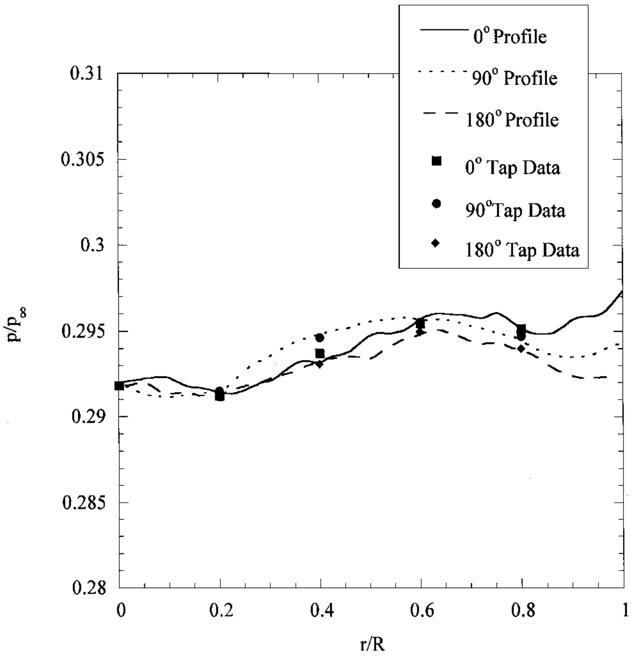

Fig. 12 Base-surface radial pressure profiles.

Observation of the entire base pressure distribution in Fig. 13 confirms the small changes in pressure across the entire base, for which the maximum variation is only 4.5%. However, the small pressure variations seen in the contour map agree qualitatively with the surface-flow pattern observed in the oil-streak visualizations already presented in Fig. 10. The general windward-to-leeward surface flow trend suggested by the oil flow is confirmed by the slightly higher base pressure on the windward portion of the base compared to that on the leeward side. In addition, the lowest surface pressure on the entire base is observed along the leeward edge between about $\phi = \pm 100$ and 180 deg, agreeing with the region where flow separates from the base surface as it is entrained by the free shear layer. The three radial base pressure profiles in Fig. 12 indicate a general small increase from the base center outward, with the pressure at the base edge highest on the windward side and lowest on the leeward side. This slight radial pressure increase of approximately 4.5% is similar to that observed at zero angle of attack, where a 3.9% increase in base pressure was observed between the base center and edge.[3]

Using 71,291 equal-sized pixels of PSP data across the base, the mean base-to-freestream static pressure ratio is calculated as $p_b / p_\infty = 0.293$. This base pressure ratio corresponds to an average base pressure coefficient of $(C_p)_b = -0.167$, where $(C_p)_b$ is defined as follows:

$$(C_p)_b = 2[(p_b / p_\infty) - 1] | \gamma M_\infty^2 \tag{2}$$

This base pressure coefficient is 63.7% lower than in the zero-angle-of-attack case,[3] corresponding to a reduction in the base pressure ratio, p_b / p_∞, of 48.4%. Regardless of the method used to report the base pressure, it is obviously significantly reduced for flight at 10-deg angle of attack, resulting in greatly increased base drag. Figure 14 compares the measured average base-pressure ratio in the current experiment to the data found by Moore et al.[15] for a tangent–ogive forebody with a cylindrical afterbody such that $L / R = 14.4$. The current data point falls quite neatly onto the Mach 2.5 curve at 10-deg angle of attack. This agreement may be purely coincidental, however, because the Moore et al. data correspond to a tangent–ogive cylindrical body with a pointed nose and $L / R = 14.4$, whereas

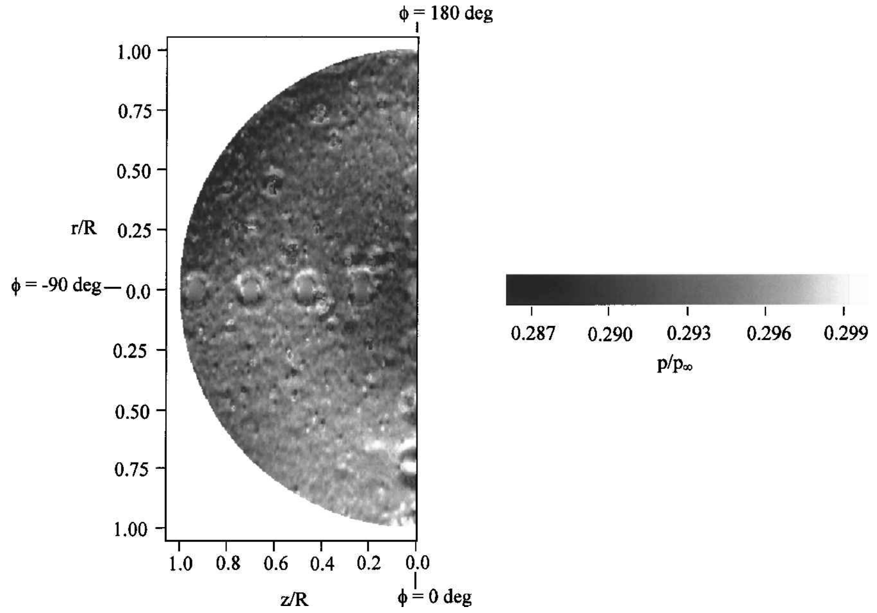

Fig. 13 Base-surface pressure contour map.

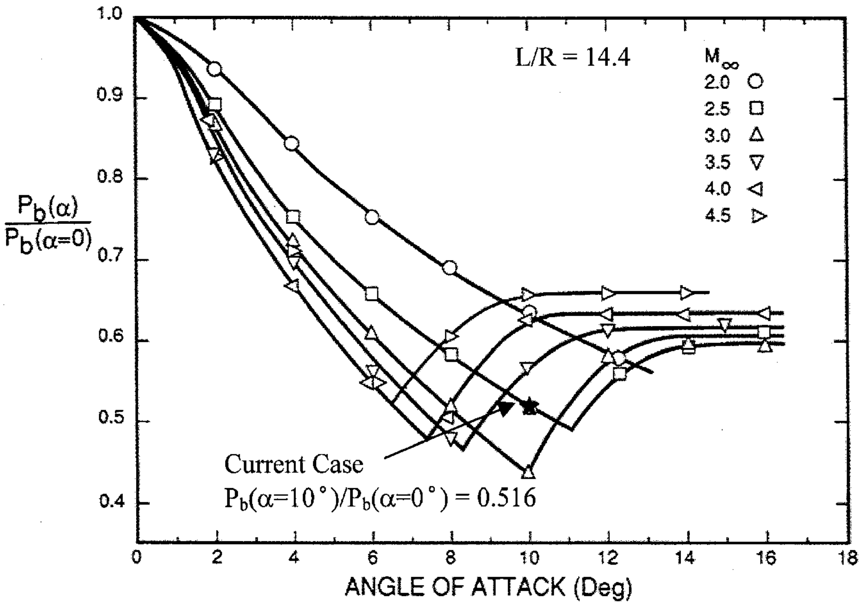

Fig. 14 Average base pressure comparison with data from Moore et al.[15] (reproduced from Ref. 13).

the current geometry consists of a 10-deg turn of a constant-diameter sting with $L/R = 3.0$. It is also possible that this agreement suggests a weak dependence of base pressure on L/R in comparison to its dependence on α and Mach number. The average base pressure can also be compared to the data of Pick,[14] although the Pick pressure data were measured at hypersonic speeds. Pick showed that for 10-deg angle of attack, the average base pressure ratio approaches $p_b/p_\infty \approx 0.2$ as the Mach number decreases toward 5, a value 32% lower than the base pressure ratio measured in this investigation. Although direct comparison between the two studies is difficult because of the large difference in Mach number between the test cases, the Pick data do show an important trend also observed in the current investigation. In the Pick results, the base pressure ratio is seen to decrease by approximately 50% at 10-deg angle of attack compared to the results measured at 0-deg angle of attack, agreeing with the 48.4% decrease measured in the current investigation and the results of Moore et al.[15] shown in Fig. 14. This trend illustrates the critical role that angle of attack plays in reducing the base pressure and, thus, increasing the overall drag, on aerodynamic bodies.

Conclusions

The supersonic Mach 2.46 flow about a cylindrical afterbody at a 10-deg angle of attack has been studied using schlieren photography, Mie scattering visualization, oil-streak surface visualization, and PSP measurements. This study permits interpretation of the general structure of this three-dimensional, separated, compressible flow and provides understanding of the fluid dynamic processes that occur for cylindrical base flows when inclined at angle of attack. Based on the visualization images and surface-pressure measurements, the following conclusions may be drawn:

1) Mean-flow gasdynamic structures appear qualitatively similar to the zero-angle-of-attack case but are rotated approximately to the afterbody angle of attack. These structures include Prandlt–Meyer expansions centered at the base corner, a free shear layer, an enclosed recirculation region, recompression shocks, and a trailing wake. In addition, large-scale turbulent structures in the recirculation and trailing wake regions resemble the structures observed in the zero-angle-of-attack case.

2) Although no flow separation appears to occur along the afterbody, the three dimensionality of the flowfield created by the 10-deg-angle-of-attack results in the development of symmetric three-dimensional lee-side vortex lobes in the near wake that complicate the separated flow structure compared to the zero-angle-of-attack case. Detailed investigation of the interaction of these vortex lobes with the base recirculation region is needed to determine their effect on the flow behavior.

3) Surface-flow visualization along the afterbody provides evidence as to the strength of the three dimensionality for Mach 2.5 flow at 10-deg angle of attack. The convergence of surface streaklines along the lee side of the afterbody provides evidence of the strong windward-to-leeward circumferential flow around the afterbody, creating a surplus of mass on the lee side. For large enough angle of attack, approach Mach number, or afterbody length, this circumferential flow would lead to flow separation and the formation of symmetric vortices near the leeward afterbody surface. However, no visualization evidence or pressure measurements suggest that flow separation actually occurs for the current case.

4) Surface-pressure measurements along the afterbody suggest a strong circumferential pressure gradient between the windward and leeward surfaces. This gradient provides the driving force for a circumferential secondary flow, resulting in the entrainment of flow from the leeward region into the base recirculation region along the $\phi = 0/180$ deg center symmetry plane.

5) The base pressure is approximately uniform spatially, but the small changes present on the base surface serve as the driving force for a complicated base surface-flow pattern. This flow pattern is characterized by a windward saddle point and leeward node of attachment on the $\phi = 0/180$ deg line, with flow generally moving in a windward-to-leeward direction, and with outward radial flow along the base occurring in the $\phi = \pm 100$–180 deg range of the leeward edge.

6) The average base pressure ratio measured for the 10-deg angle-of-attack case is 48.4% lower than the zero-angle-of-attack case. This reduction in base pressure greatly increases the base drag for supersonic flight at angle of attack. This average base pressure ratio agrees closely with that of Moore et al.[15] for a tangent–ogive forebody at the same angle of attack, but with a much larger length-to-radius ratio ($L/R = 14.4$) than the current afterbody (3.0), although this agreement may be fortuitous.

Acknowledgments

This work is supported by the U.S. Army Research Office under Grant DAAG55-97-1-0122, with Thomas L. Doligalski as Technical Monitor. In addition, gratitude is expressed to C. J. Bourdon and M. A. Woodmansee for assistance with the Mie scattering and pressure-sensitive paint experiments, respectively.

References

[1] Heltsley, F. L., Walker, B. J., and Nichols, R. H., "Transonic Nozzle-Afterbody Flow Field Measurements Using A Laser Doppler Velocimeter," CP-348, AGARD, 1983.

[2] Berner, C., "Supersonic Base Flow Investigation over Axisymmetric Afterbodies," *Fifth International Conference on Laser Anemometry, Proceedings of SPIE: The International Society for Optical Engineering*, Vol. 2052, Society of Photo-Optical Instrumentation Engineers, Bellingham, WA, 1993, pp. 249–256.

[3] Herrin, J. L., and Dutton, J. C., "Supersonic Base Flow Experiments in the Near-Wake of a Cylindrical Afterbody," *AIAA Journal*, Vol. 32, No. 1, 1994, pp. 77–83.

[4] Herrin, J. L., and Dutton, J. C., "Supersonic Near-Wake Afterbody Boattailing Effects on Axisymmetric Bodies," *Journal of Spacecraft and Rockets*, Vol. 31, No. 6, 1994, pp. 1021–1028.

[5] Mathur, T., and Dutton, J. C., "Base-Bleed Experiments with a Cylindrical Afterbody in Supersonic Flow," *Journal of Spacecraft and Rockets*, Vol. 33, No. 1, 1996, pp. 30–37.

[6] Mathur, T., and Dutton, J. C., "Velocity and Turbulence Measurements in a Supersonic Base Flow with Mass Bleed," *AIAA Journal*, Vol. 34, No. 6, 1996, pp. 1153–1159.

[7] Reijasse, P., Corbel, B., and Delery, J., "Flow Confluence Past a Jet-On Axisymmetric Afterbody," *Journal of Spacecraft and Rockets*, Vol. 34, No. 5, 1997, pp. 593–601.

[8] Sahu, J., "Numerical Computations of Supersonic Base Flow with Special Emphasis on Turbulence Modeling," *AIAA Journal*, Vol. 32, No. 7, 1994, pp. 1547–1549.

[9] Tucker, P. K., and Shyy, W., "A Numerical Analysis of Supersonic Flow over an Axisymmetric Afterbody," AIAA Paper 93-2347, June 1993.

[10] Chuang, C.-C., and Chieng, C.-C., "Supersonic Base-Flow Computation Using Higher-Order Closure Turbulence Models," *Journal of Spacecraft and Rockets*, Vol. 33, No. 3, 1996, pp. 374–380.

[11] Fureby, C., Nilsson, Y., and Andersson, K., "Large Eddy Simulation of Supersonic Base Flow," AIAA Paper 99-0426, Jan. 1999.

[12] Oberkampf, W. L., and Bartel, T. J., "Symmetric Body Vortex Wake Characteristics in Supersonic Flow," *AIAA Journal*, Vol. 18, No. 11, 1980, pp. 1289–1297.

[13] Lamb, J. P., and Oberkampf, W. L., "Review and Development of Base Pressure and Base Heating Correlations in Supersonic Flow," *Journal of Spacecraft and Rockets*, Vol. 32, No. 1, 1993, pp. 8–23.

[14] Pick, G. S., "Base Pressure Distributions of a Cone at Hypersonic Speeds," *AIAA Journal*, Vol. 10, No. 12, 1972, pp. 1685, 1686.

[15] Moore, F. G., Hymer, T., and Wilcox, F. J., "Improved Empirical Model for Base Drag Prediction on Missile Configurations Based on New Wind Tunnel Data," U.S. Naval Surface Warfare Center, Rept. NSWCDD/TR-92/509, 1992.

[16] Sturek, W. B., Birch, T., Lauzon, M., Housh, C., Manter, J., Josyula, E., and Soni, B., "The Application of CFD to the Prediction of Missile Body Vortices," AIAA Paper 97-0637, Jan. 1997.

[17] Sahu, J., "Three Dimensional Base Flow Calculation for a Projectile at Transonic Velocity," AIAA Paper 86-1051, May 1986.

[18] Sahu, J., "Three-Dimensional Flow Calculations for a Projectile with Standard and Dome Bases," *Journal of Spacecraft and Rockets*, Vol. 31, No. 1, 1994, pp. 106–111.

[19] Herrin, J. L., "An Experimental Investigation of Supersonic Axisymmetric Base Flow Including the Effects of Afterbody Boattailing," Ph.D. Dissertation, Dept. of Mechanical and Industrial Engineering, Univ. of Illinois, Urbana, IL, July 1993.

[20] Smith, K. M., and Dutton, J. C., "Investigation of Large-Scale Structures in Supersonic Planar Base Flows," *AIAA Journal*, Vol. 34, No. 6, 1996, pp. 1146–1152.

[21] Bloomberg, J. E., "An Investigation of Particle Dynamics Effects Related to LDV Measurements in Compressible Flows," M.S. Thesis, Dept. of Mechanical and Industrial Engineering, Univ. of Illinois, Urbana, IL, May 1989.

[22] Kavandi, J., Callis, J., Gouterman, M., Khalil, G., Wright, D., Green, E., Burns, D., and McLachlan, B., "Luminescent Barometry in Wind Tunnels," *Review of Scientific Instruments*, Vol. 61, No. 11, 1990, pp. 3340–3347.

[23] Morris, M. J., Donovan, J. F., Kegelman, J. T., Schwab, S. D., Levy, R. L., and Crites, R. C., "Aerodynamic Applications of Pressure-Sensitive Paint," *AIAA Journal*, Vol. 31, No. 3, 1993, pp. 419–425.

[24] Woodmansee, M. A., and Dutton, J. C., "Treating Temperature-Sensitivity Effects of Pressure-Sensitive Paint Measurements," *Experiments in Fluids*, Vol. 24, No. 2, 1998, pp. 163–174.

[25] Woodmansee, M. A., "Temperature-Sensitivity Effects of Pressure-Sensitive Paint and Associated Wind Tunnel Data Reduction Methods," M.S. Thesis, Dept. of Mechanical and Industrial Engineering, Univ. of Illinois, Urbana, IL, Jan. 1997.

[26] Sun, C. C., and Childs, M. E., "A Modified Wall Wake Velocity Profile for Turbulent Compressible Boundary Layers," *Journal of Aircraft*, Vol. 10, No. 6, 1973, pp. 381–383.

[27] Fernholz, H. H., and Finley, P. J., "A Critical Commentary on Mean Flow Data for Two-Dimensional Compressible Turbulent Boundary Layers," AGARDograph 253, 1980.

[28] Bourdon, C. J., and Dutton, J. C., "Planar Visualizations of Large-Scale Turbulent Structures in Axisymmetric Supersonic Separated Flows," *Physics of Fluids*, Vol. 11, No. 1, 1999, pp. 201–213.

[29] Tobak, M., and Peake, D. J., "Topology of Three-Dimensional Separated Flows," *Annual Review of Fluid Mechanics*, Vol. 14, 1982, pp. 61–85.

R. P. Lucht
Associate Editor